Signatures of topological phase transition on a quantum critical line

Ranjith R. Kumar,[1,2] Nilanjan Roy,[3] Y. R. Kartik,[1,2] S. Rahul,[1,2] and Sujit Sarkar[1]
[1]*Theoretical Sciences Division, Poornaprajna Institute of Scientific Research, Bidalur, Bengaluru-562164, India*
[2]*Graduate Studies, Manipal Academy of Higher Education, Madhava Nagar, Manipal-576104, India*
[3]*Centre for Condensed Matter Theory, Department of Physics, Indian Institute of Science, Bengaluru-560012, India*

(Received 19 April 2022; revised 20 April 2023; accepted 25 April 2023; published 9 May 2023)

Recently topological states of matter have witnessed a new physical phenomenon where both edge modes and gapless bulk coexist at topological quantum criticality. The presence and absence of edge modes on a critical line can lead to an unusual class of topological phase transition between the topological and nontopological critical phases. We explore the existence of this new class of topological phase transitions in a generic model representing the topological insulators and superconductors and we show that such transition occurs at a multicritical point, i.e., at the intersection of two critical lines. To characterize these transitions we reconstruct the theoretical frameworks, which include bound state solution of the Dirac equation, winding number, correlation factors, and scaling theory of the curvature function to work for the criticality. Critical exponents and scaling laws are discussed to distinguish between the multicritical points, which separate the critical phases. Entanglement entropy and its scaling in the real space provide further insights into the unique transition at criticality revealing the interplay between fixed point and critical point at the multicriticalities.

DOI: 10.1103/PhysRevB.107.205114

I. INTRODUCTION

In the quest of classifying novel phases of quantum matter in the absence of local order parameters, the topology of electronic band structure plays a prime role [1–4]. It enables the distinction between gapped phases in terms of a quantized invariant number, which counts the number of localized edge modes present [5]. The transition between the distinct topological phases involves a bulk band gap closing at the point of topological phase transition. Across the transition the number of edge modes, protected by the bulk gap, changes [6]. In the gapped phases, the localization length of the edge modes diverges as the system drives towards the transition point or criticality [7].

Interestingly, this conventional knowledge is revised recently, realizing even criticalities can host the stable localized edge modes despite the vanishing bulk gap [8–19]. This results in the emergence of nontrivial criticalities with unique topological properties even in the presence of gapless bulk excitations. The nontrivial criticalities can be effectively characterized in terms of the zeros and poles of complex function associated with the Hamiltonian [8]. The localized edge modes at criticality are protected by novel phenomena such as kinetic inversion [11] (in fermionic models) and finite high-energy charge gap [16] (in bosonic models). It has been shown that they also remain robust against interactions and disorders [8,9]. This intriguing interplay between topology and criticality causes an unconventional topological transition between critical phases [11,20].

In this work, we report the possibility of a new kind of topological phase transition between critical phases, happening at a multicritical point where two critical lines intersect. Considering a two-band model as a prototype representing gapless (critical) topological insulators and superconductors, in Sec. II we find the critical lines in the model and existence of two species of multicritical points with quadratic and linear dispersions, both corresponding to the topological transition between distinct critical phases. In support of our finding, in Sec. III, we solve the Dirac equation for criticality to obtain the localized edge mode solutions in the nontrivial critical phases. This is further supported by our proposal of obtaining the nonzero integer winding number for nontrivial critical phases, which we discuss in Sec. IV A. This proposal is supported in Sec. IV B by calculating the winding number using zeros and poles of a complex function. The curvature function diverges on approaching the multicritical points from critical phases indicating the existence of a transition between critical phases. The critical exponents (γ, ν, z), discussed in Sec. V A, unravel the different universality classes of two multicritical points. Using the divergence of curvature function we develop a renormalization group (RG) scheme to distinguish the different critical phases in Sec. V B. In Sec. V C we show that a correlation length, extracted from the Fourier-transformed curvature function, diverges at the multicritical points indicating phase transitions between critical phases. Further, in Sec. VI we study the spatial scaling of entanglement entropy, especially to characterize and distinguish the multicritical points. The scaling reveals an interplay between the fixed points and multicritical points. The entanglement entropy is minimum where the fixed point and multicritical point overlap reflecting the dominance of the former over the latter. Finally, we conclude in Sec. VII.

II. MODEL

We consider a one-dimensional (1D) lattice chain of spinless fermions in momentum space [21,22] represented by a generic two-band Bloch Hamiltonian of the form

$$\mathcal{H}(k, \mathbf{\Gamma}) = \boldsymbol{\chi}.\boldsymbol{\sigma} = \chi_x \sigma_x + \chi_y \sigma_y, \tag{1}$$

where $\mathbf{\Gamma} = \{\Gamma_0, \Gamma_1, \Gamma_2\}$, $\chi_x = \Gamma_0 + \Gamma_1 \cos k + \Gamma_2 \cos 2k$, and $\chi_y = \Gamma_1 \sin k + \Gamma_2 \sin 2k$ and $\boldsymbol{\sigma} = (\sigma_x, \sigma_y)$ are the Pauli matrices. The model represents extended Su-Schrieffer-Heeger (SSH) [23] and extended Kitaev models [24] by uniquely defining the parameters (see Appendix A for detailed discussion on the physical relevance of the model). The parameters Γ_0, Γ_1, and Γ_2 describe the on-site potential, the nearest-neighbor (NN) couplings, and the next-nearest-neighbor (NNN) couplings, respectively.

In general, the model can support three distinct gapped phases distinguished by the number of edge modes they possess. These phases can be identified with the winding numbers $w = 0$, 1, and 2, which quantify the edge modes. The model undergoes transition between these phases with necessarily involving the gap closing, $E_k = \pm\sqrt{\chi_x^2+\chi_y^2}=0$, at the phase boundaries. The criticalities, where the bulk gap closes, occurs for the momentum $k_0 = 0, \pm\pi, \cos^{-1}(-\Gamma_1/2\Gamma_2)$, which, respectively, gives the critical surfaces $\Gamma_1 = -(\Gamma_0 + \Gamma_2)$, $\Gamma_1 = (\Gamma_0 + \Gamma_2)$, and $\Gamma_0 = \Gamma_2$. The model possesses three multicritical lines at which two critical surfaces intersect. Two of them (MC_1) share identical properties and show quadratic dispersion around the gap closing point and the other one (MC_2) is identified with the linear dispersion. Uniquely, the model supports the edge modes and topological transition at critical surfaces $\Gamma_1 = \pm(\Gamma_0 + \Gamma_2)$ corresponding to $k_0 = \pi, 0$, respectively (see Appendix B for the numerical results).

To further explore these unique phenomena we propose a framework that works out for criticality without referring to any of the gapped phases of the model. Ideally driving the system to criticality involves $k \to k_0$ and $\mathbf{\Gamma} \to \mathbf{\Gamma}_c$, where $\mathbf{\Gamma}_c$ is the critical point in the parameter space. To avoid the singularities involving the exact critical point, one can define the Hamiltonian critical only in the parameter space as $\mathcal{H}(k, \mathbf{\Gamma}_c)$ with $k = k_0 + \Delta k$, where $\Delta k \ll 2\pi$. This situation is hereafter referred to as criticality in this work.

The model at criticality can be obtained by using the critical surface relation, which modifies the components into $\chi_x = \Gamma_0(1 + \cos k) + \Gamma_2(\cos 2k + \cos k)$ and $\chi_y = \Gamma_2(\sin 2k + \sin k) + \Gamma_0 \sin k$ for $\Gamma_1 = (\Gamma_0 + \Gamma_2)$ and $\chi_x = \Gamma_0(1 - \cos k) + \Gamma_2(\cos 2k - \cos k)$ and $\chi_y = \Gamma_2(\sin 2k - \sin k) - \Gamma_0 \sin k$ for $\Gamma_1 = -(\Gamma_0 + \Gamma_2)$. The possible topological trivial and nontrivial critical phases are separated by the phase boundaries at the multicritical lines $\Gamma_2 = \Gamma_0$ (MC_1) and $\Gamma_2 = -\Gamma_0$ (MC_2). Without loss of any generality, we assume $\Gamma_0 = 1$. Hence hereafter the critical surfaces and the multicritical lines will be called as the critical lines and the multicritical points, respectively, as shown in Fig. 1(a). The multicriticalities, $MC_{1,2}$, are identified with quadratic and linear dispersion, respectively, as shown in Fig. 1(b). They can be obtained for the following k_0^{mc}. For $\Gamma_2 = \Gamma_0$ (MC_1):

$$k_0^{mc} = \cos^{-1}\left(-\frac{\Gamma_2 + \Gamma_0}{2\Gamma_2}\right) \quad \text{at} \quad \Gamma_1 = (\Gamma_0 + \Gamma_2), \tag{2}$$

$$k_0^{mc} = \cos^{-1}\left(\frac{\Gamma_2 + \Gamma_0}{2\Gamma_2}\right) \quad \text{at} \quad \Gamma_1 = -(\Gamma_0 + \Gamma_2). \tag{3}$$

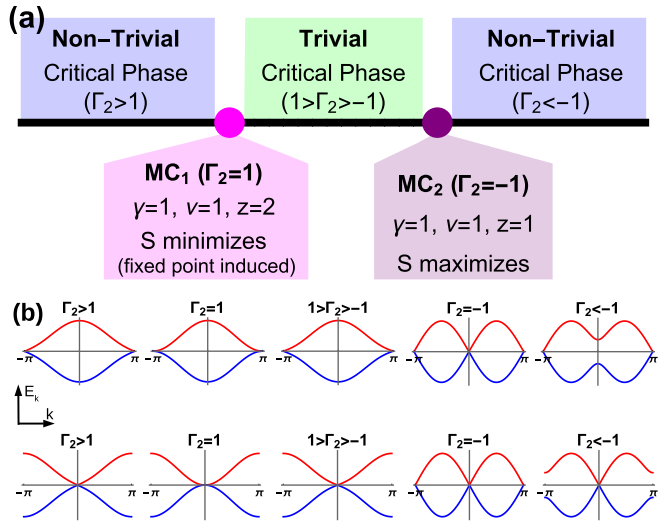

FIG. 1. (a) Schematic representation of both the criticalities $\Gamma_1 = \pm(\Gamma_0 + \Gamma_2)$ with $\Gamma_0 = 1$. Nontrivial critical phases: $1 < \Gamma_2$ and $\Gamma_2 < -1$ (solid lines), trivial critical phase: $1 > \Gamma_2 > -1$ (dashed line) are separated by the multicriticalities $MC_{1,2}$. The entanglement entropy (S) minimizes at MC_1, which is also an RG fixed point, and maximizes at MC_2. The $MC_{1,2}$ belongs to the universality classes obtained from the exponents $(\gamma, \nu, z) = (1, 1, 2)$ and $(\gamma, \nu, z) = (1, 1, 1)$ respectively. (b) Dispersion at different critical phases and multicritical points. Top: on the critical line for $k_0 = \pm\pi$. Bottom: on the critical line for $k_0 = 0$.

For $\Gamma_2 = -\Gamma_0$ (MC_2):

$$k_0^{mc} = 0 \quad \text{at} \quad \Gamma_1 = (\Gamma_0 + \Gamma_2), \tag{4}$$

$$k_0^{mc} = \pi \quad \text{at} \quad \Gamma_1 = -(\Gamma_0 + \Gamma_2). \tag{5}$$

Interestingly, MC_2 exhibits swapping of the values of k_0^{mc}. At MC_2, one can observe that $k_0^{mc} = 0$ for $\Gamma_1 = (\Gamma_0 + \Gamma_2)$, which was obtained for $k_0 = \pi$ and $k_0^{mc} = \pi$ for $\Gamma_1 = -(\Gamma_0 + \Gamma_2)$, which was obtained for $k_0 = 0$. This property emerge as a result of intersection of both the critical lines at MC_2. We will show in the following that our proposed framework based on the near-critical Hamiltonian $\mathcal{H}(k, \mathbf{\Gamma}_c)$ can capture the essential physics of topological transition at criticality.

III. BOUND STATE SOLUTION OF THE DIRAC EQUATION

The presence of edge modes in topological insulators and superconductors is lucid from the bound state solution of Dirac equation [25–27]. We solve the model in Eq. (1) for the bound state solution at criticality (see Appendix C for the bound state solution at gapped phases). Interestingly, as a consequence of the near-critical approach adopted here, the Dirac Hamiltonian at criticality naturally fixes the interface at a multicritical point. Dirac Hamiltonian at criticality up to third-order expansion around k_0^{mc} for MC_1 is

$$\mathcal{H}(k) \approx \epsilon_1 k^2 \sigma_x + (\epsilon_2 k - \epsilon_3 k^3)\sigma_y. \tag{6}$$

where $\epsilon_1 = (\Gamma_0 - 3\Gamma_2)/2$, $\epsilon_2 = (\Gamma_2 - \Gamma_0)$, and $\epsilon_3 = (7\Gamma_2 - \Gamma_0)/6$. We look for zero-energy solution in real space (we set $\hbar = 1$ throughout the discussion), $\mathcal{H}\psi(x) = 0$. Identifying the spinor of the wave function $\psi(x) = \rho_\eta \phi(x)$ is an eigenstate

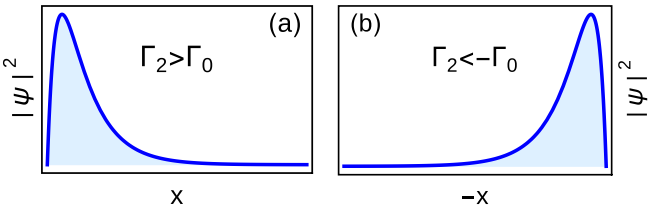

FIG. 2. Bound state solutions of the edge modes at the non-trivial critical phases. (a) Plotted for $\Gamma_2 = 3\Gamma_0$ (with $\Gamma_0 = 1$) at the critical phase $\Gamma_2 > \Gamma_0$. (b) Plotted for $\Gamma_2 = -3\Gamma_0$ (with $\Gamma_0 = 1$) at the critical phase $\Gamma_2 < -\Gamma_0$.

of σ_z and using $\phi(x) \propto e^{-x/\xi}$, inverse of the nonzero decay length can be obtained as $\xi_\pm^{-1} = (-\eta\epsilon_1 \pm \sqrt{\epsilon_1^2 - 4\epsilon_2\epsilon_3})/(-2\epsilon_3)$. For both roots to be positive, it requires $\xi_+^{-1} + \xi_-^{-1} > 0$, which implies $\eta = \text{sign}(\epsilon_1/\epsilon_3)$. The edge mode decay length (longer one of two) is $\xi_+ \approx |\epsilon_1|/\epsilon_2$ remains finite and positive for $\epsilon_2 > 0$, i.e., $\Gamma_2 > \Gamma_0$, which means the criticality in this region possesses edge modes and is the topological nontrivial phase. Note that the term ϵ_2 is the gap term at criticality, which mimics the role of mass. As $\epsilon_2 \to 0$ the decay length $\xi_+ \to \infty$ indicating the edge mode delocalize into the bulk and topological transition takes place at MC_1, i.e., at $\Gamma_2 = \Gamma_0$. To visualize this phenomenon we write the bound state solution $\psi(x) \propto (\eta \quad 0)^T (e^{-x/\xi_+} - e^{-x/\xi_-})$, which distributes dominantly near the boundary and decay exponentially as $x \to \infty$, as shown in Fig. 2(a).

To identify the topological transition at MC_2 and the corresponding topological nontrivial phase one has to consider the swapping property of k_0^{mc}, which emerge as a result of intersection of critical lines at MC_2. In this case, after expanding around k_0^{mc} and using the swapping property, the Dirac Hamiltonian can be obtained up to second order as

$$\mathcal{H}(k) \approx (\epsilon_1 - \epsilon_3 k^2)\sigma_x + (-i\epsilon_2 k)\sigma_y, \tag{7}$$

where $\epsilon_1 = 2(\Gamma_0 + \Gamma_2)$, $\epsilon_2 = (\Gamma_0 + 3\Gamma_2)$, and $\epsilon_3 = (5\Gamma_2 + \Gamma_0)/2$. With $\eta = \text{sign}(\epsilon_2/\epsilon_3)$, the edge mode decay length $\xi_+ \approx -(|\epsilon_2|/\epsilon_1)$ is obtained using $\phi(x) \propto e^{x/\xi}$ and is positive if $\epsilon_1 < 0$. Therefore, in this case, the gap term is ϵ_1, which vanishes at the multicritical point MC_2, i.e., at $\Gamma_2 = -\Gamma_0$. This implies that the criticality $\Gamma_2 < -\Gamma_0$ is topological nontrivial phase and the topological transition occur at MC_2, i.e., $\Gamma_2 = -\Gamma_0$ as a consequence of the delocalization of edge mode into the bulk as $\epsilon_1 \to 0$. In this case the bound state solution $\psi(x) \propto (0 \quad \eta)^T (e^{x/\xi_+} - e^{x/\xi_-})$, distributes near the boundary and decay as $x \to -\infty$ as shown in Fig. 2(b).

IV. WINDING NUMBER

The topological character of a gapped phase is quantified using topological invariant numbers [5]. The quantized values of these invariant numbers represents the number of localized stable edge modes at each end of the open chain. For one-dimensional systems winding number is a good invariant number, which represents the winding of pseudospin vector in the Brillouin zone [28]. Therefore, the edge excitations of the gapped phases can be quantified in terms of winding

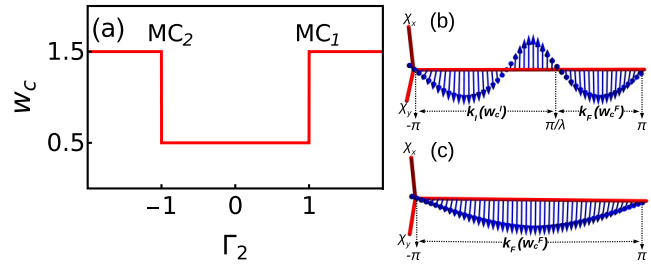

FIG. 3. Winding number at criticality. (a) Fractional values of winding number (w_c). Trivial critical phases are identified with $w_c = 0.5$ and nontrivial critical phases are identified with $w_c = 1.5$. The topological transition occurs at the multicritical points $MC_{1,2}$, i.e,, $\Gamma_2 = \pm\Gamma_0$ with $\Gamma_0 = 1$. (b) Winding of unit vector $\hat{\boldsymbol{\chi}}$ at nontrivial critical phases with both integer (w_c^I) and fractional parts (w_c^F). (c) Winding of $\hat{\boldsymbol{\chi}}$ at the trivial critical phase with only fractional part (w_c^F).

number [6]

$$w = \frac{1}{2\pi} \oint_{BZ} F(k, \boldsymbol{\Gamma}) dk, \tag{8}$$

where $F(k, \boldsymbol{\Gamma}) = i\langle u_k | \partial_k | u_k \rangle$ is the Berry connection or curvature function of Bloch wave function $\psi_k(r) = u_k(r)e^{ikr}$.

In order to quantify the edge modes at criticality one has to define the winding number at criticality [11]. The conventional definition of winding number fails at criticalities. This is due to the nonanalyticity of the curvature function [integrand in Eq. (8)] at criticalities. This constraint is naturally avoided in the near-critical approach and allows one to calculate the winding number in its usual integral form even at criticality.

$$w_c = \frac{1}{2\pi} \lim_{\delta \to 0} \oint_{|k-k_0|>\delta} F(k, \boldsymbol{\Gamma}_c) dk. \tag{9}$$

However, it yields fractional values, as shown in Fig. 3(a), which does not account correctly for the number of edge modes present at criticalities.

Alternatively, one can refer to the auxiliary space and differentiate between NN and NNN loops and consider only one among them, which gives integer contribution and accounts for the edge modes at criticality [12]. However, this method is not efficient as the auxiliary space loops gets complicated with the increasing NN couplings [28].

A. Winding number at criticality

The fractional values at criticality imply the presence of fractional winding of unit vector $\hat{\boldsymbol{\chi}} = \boldsymbol{\chi}/|\boldsymbol{\chi}|$, in the auxiliary space over the Brillouin zone [11,12,28]. For nontrivial critical phases, one can identify integer winding (w_c^I) of the unit vector along with an extended fractional winding (w_c^F) in the Brillouin zone, as shown in Fig. 3(b). For trivial criticalities, only fractional winding can be observed as in Fig. 3(c). Based on this, we propose that the winding number at criticality should be approximated to only the integer values, which effectively captures the number of edge modes at criticality.

Proposition. Winding number at criticality (w_c), which acquires fractional values ($w_c = w_c^I + w_c^F$), can be effectively approximated only to its integer part, i.e., $w_c \approxeq w_c^I$, to quantify the number of edge modes present at criticality.

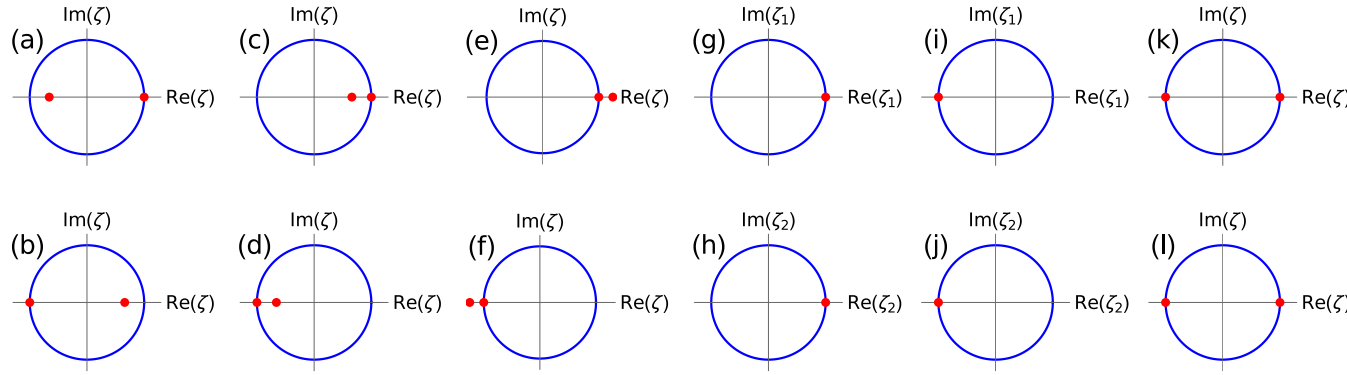

FIG. 4. Zeros ($\zeta_{1,2}$) of the complex function in Eq. (12), i.e., $\zeta_1 = 1$, $\zeta_2 = \Gamma_0/\Gamma_2$ for $\Gamma_1 = -(\Gamma_0 + \Gamma_2)$ and $\zeta_1 = -1$, $\zeta_2 = -\Gamma_0/\Gamma_2$ for $\Gamma_1 = (\Gamma_0 + \Gamma_2)$, represented as red dots. (a), (b) Winding number $w = N_z - N_p = 1$ at nontrivial critical phase with $\Gamma_0 = 1$ and $\Gamma_2 = -1.5$. (c), (d) Winding number $w = 1$ at nontrivial critical phase with $\Gamma_0 = 1$ and $\Gamma_2 = 1.5$. (e), (f) Winding number $w = 0$ at trivial critical phase with $\Gamma_0 = 1$ and $\Gamma_2 = 0.5$. (g), (h), (i), (j) Degenerate zeros on the unit circle at MC_1, for (g), (h) the critical line $\Gamma_1 = -(\Gamma_0 + \Gamma_2)$ and (i), (j) the critical line $\Gamma_1 = (\Gamma_0 + \Gamma_2)$. (g), (h), (i), (j) indicate the multicritical point MC_1 has multiplicity $m = 2$ and dynamical exponent $z = 2$ [8]. (k), (l) Zeros at MC_2. Both the zeros lie on the unit circle and are nondegenerate. The top and bottom panels are for $\Gamma_1 = \mp(\Gamma_0 + \Gamma_2)$, respectively.

The proposal roots in the fact that the momentum zones can be divided into integer and fractional windings as $-\pi < k_I < \pi/\lambda$ and $\pi/\lambda < k_F < \pi$, respectively. The cutoff λ differentiates the momentum zones responsible for integer and fractional windings of the unit vector, as shown in Fig. 3(b). Therefore, we write

$$w_c = \frac{1}{2\pi} \lim_{\delta \to 0} \left(\int_{\substack{-\pi \\ |k-k_0|>\delta}}^{\pi/\lambda} F(k, \mathbf{\Gamma}_c) dk + \int_{\substack{\pi/\lambda \\ |k-k_0|>\delta}}^{\pi} F(k, \mathbf{\Gamma}_c) dk \right)$$
$$= w_c^I + w_c^F \approxeq w_c^I. \tag{10}$$

The fractional winding can be found to have $w_c^F = 1/2$ since the critical phases have one gap closing point in the Brillouin zone. The interger winding $w_c^I \in \mathbb{Z}$ counts the number of edge modes in the corresponding critical phase. The winding number in the nontrivial critical phases of the model can be found to have $w_c = 1.5$, for which the corresponding $w_c^I = 1$. Hence w_c^I correctly accounts for one edge mode living at the criticalities, which we also find from the solution of the Dirac equation. For the trivial critical phase $w_c = 0.5$ and $w_c^I = 0$ implying no localized edge modes. The transition between the critical phases with $w_c^I = 0$ and $w_c^I = 1$ occur at the multicritical points. This clearly demonstrates the topological transition at criticality through multicritical points.

The proposal can be found viable for the critical systems that support nontrivial critical phases having the winding number $w_c > 2$ and characterized with a single gap closing point. The models with couplings beyond the second neighbor [29] support the nontrivial critical phases with winding numbers $w_c = 2.5, 3.5, \ldots$, etc. In the case of $w_c = 2.5$, the unit vector $\hat{\boldsymbol{\chi}}$ winds twice with an extended fractional winding in the Brillouin zone. The approximation to only the integer value yields $w_c^I = 2$, which counts the two edge modes localized in the corresponding critical phase. Therefore, we expect that the proposition will be useful in characterizing the nontrivial critical phases with higher winding numbers and a single gap closing point. For more than one gap closing point in the Brillouin zone, such as the non-high-symmetry points discussed in Ref. [29], the proposition might need further modification.

B. Winding number using zeros and poles

The proposal and the integer winding number w_c^I can be found consistent with the method used in Ref. [8], where the winding number is defined using number of zeros (N_z) and order of poles (N_p), $w = N_z - N_p$. The zeros and poles of a complex function is obtained by writing the fermionic creation and annihilation operators in terms of Majorana operators and followed by a Fourier transformation. With the substitution $e^{ik} = \zeta$, (where ζ is a complex number) where e^{ik} goes around the unit circle in the complex plane as k varies over the Brillouin zone, we get the complex function $f(\zeta)$ living on the unit circle in the complex plane

$$f(\zeta) = \sum_{\mu=-\infty}^{\infty} t_\mu \zeta^\mu. \tag{11}$$

For extended Kitaev model it reads $f(\zeta) = \sum_{\mu=0}^{2} t_\mu \zeta^\mu$ [with no poles) where $t_{0,1,2}$ are, respectively, $-\beta_0, \beta_1, \beta_2$ (parameters of Kitaev model in Eq. (A2)]. Using the mapping $2\beta_0 = \Gamma_0$, $-2\beta_1 = \Gamma_1$, and $-2\beta_2 = \Gamma_2$ one can write the complex function for the generic model

$$f(\zeta) = -\frac{\Gamma_0}{2} - \frac{\Gamma_1}{2}\zeta - \frac{\Gamma_2}{2}\zeta^2. \tag{12}$$

The solutions are $\zeta_{1,2} = (\Gamma_1 \pm \sqrt{\Gamma_1^2 - 4\Gamma_0\Gamma_2})/-2\Gamma_2$. To characterize the topological trivial and nontrivial critical phases we write the solution at criticalities. For $\Gamma_1 = -(\Gamma_0 + \Gamma_2)$ we get $\zeta_1 = 1$, $\zeta_2 = \Gamma_0/\Gamma_2$ and for $\Gamma_1 = (\Gamma_0 + \Gamma_2)$ we get $\zeta_1 = -1$, $\zeta_2 = -\Gamma_0/\Gamma_2$.

It is evident that one of the zeros lies on the unit circle since the system is critical and the other zero falls inside (outside) the unit circle for topological nontrivial (trivial) critical phase, as shown in Fig. 4. Winding number is determined by the number of zeros falling inside the unit circle, whose value can be found consistent with w_c^I. For nontrivial critical phases as

shown in Figs. 4(a)–4(d) (where top and bottom panels represent $\Gamma_1 = \mp(\Gamma_0 + \Gamma_2)$, respectively), $w = w_c^I = 1$ and for trivial critical phases as shown in Figs. 4(e), 4(f) $w = w_c^I = 0$.

At MC_1, the zeros can be obtained to be degenerate (with multiplicity m), i.e., $\zeta_{1,2} = 1$ in Figs. 4(g), 4(h) and $\zeta_{1,2} = -1$ in Figs. 4(i), 4(j) on the critical lines $\Gamma_1 = -(\Gamma_0 + \Gamma_2)$ and $\Gamma_1 = (\Gamma_0 + \Gamma_2)$, respectively. At MC_2, we get nondegenerate zeros with $\zeta_{1,2} = \pm 1$ for both the criticalities, as shown in Figs. 4(k), 4(l).

V. CURVATURE FUNCTION

Topological phase transition can be induced by changing the underlying topology of the system upon tuning the parameters $\mathbf{\Gamma}$ appropriately. The information of the topological property of the system is embedded in the curvature function $F(k, \mathbf{\Gamma})$ defined at momentum k [30–41]. The topological quantum phase transition can be identified from the quantized jump of topological invariant number as the parameter tuned across the critical point $\mathbf{\Gamma}_c$. As the system approaches critical point to undergo topological phase transition, i.e,, $\mathbf{\Gamma} \to \mathbf{\Gamma}_c$, curvature function diverges at k_0, with the diverging curve satisfying $F(k_0 + \delta k, \mathbf{\Gamma}) = F(k_0 - \delta k, \mathbf{\Gamma})$. The sign of the diverging peak flips across the critical point as

$$\lim_{\mathbf{\Gamma} \to \mathbf{\Gamma}_c^+} F(k_0, \mathbf{\Gamma}) = -\lim_{\mathbf{\Gamma} \to \mathbf{\Gamma}_c^-} F(k_0, \mathbf{\Gamma}) = \pm\infty. \tag{13}$$

Interestingly, even at criticality, the qualitative behavior of the curvature function remains the same with the fact that now the critical point is a multicriticality, which governs the topological transition between critical phases. As one tunes the parameters at criticality $\mathbf{\Gamma}_c$ towards a multicritical point $\mathbf{\Gamma}_{mc}$, the curvature function diverges at k_0^{mc} with the symmetric nature $F(k_0^{mc} + \delta k, \mathbf{\Gamma}_c) = F(k_0^{mc} - \delta k, \mathbf{\Gamma}_c)$, as shown in Fig. 5(a).

Topological transition is signaled as the sign of the diverging peak flips if the parameters tuned across the multicritical point.

$$\lim_{\mathbf{\Gamma}_c \to \mathbf{\Gamma}_{mc}^+} F\left(k_0^{mc}, \mathbf{\Gamma}_c\right) = -\lim_{\mathbf{\Gamma}_c \to \mathbf{\Gamma}_{mc}^-} F\left(k_0^{mc}, \mathbf{\Gamma}_c\right) = \pm\infty. \tag{14}$$

This is the characteristic feature of topological transition at criticality through both the multicritical points $MC_{1,2}$. The curvature function of the generic model at criticality can be written using the critical line relations of the parameters. The pseudo-spin-vectors on the two critical lines, $\Gamma_1 = \pm(\Gamma_0 + \Gamma_2)$, of the model are $\chi_x(k) = \Gamma_0(1 \pm \cos k) + \Gamma_2(\cos 2k \pm \cos k)$, and $\chi_y(k) = \Gamma_2(\sin 2k \pm \sin k) \pm \Gamma_0 \sin k$. This defines curvature function on the critical lines $F(k, \mathbf{\Gamma}_c) = F(k, \mathbf{\Gamma}_{\Gamma_1 = \pm(\Gamma_0 + \Gamma_2)})$,

$$\begin{aligned} F\left(k, \mathbf{\Gamma}_{\Gamma_1 = \pm(\Gamma_0 + \Gamma_2)}\right) &= \frac{\chi_x \partial_k \chi_y - \chi_y \partial_k \chi_x}{\chi_x^2 + \chi_y^2} \\ &= \frac{\Gamma_0^2 + 3\Gamma_2^2 \pm 4\Gamma_0\Gamma_2 \cos k}{2\left(\Gamma_0^2 + \Gamma_2^2 \pm 2\Gamma_0\Gamma_2 \cos k\right)}. \end{aligned} \tag{15}$$

The property in Eq. (14) can be observed to be obeyed by $F(k, \mathbf{\Gamma}_{\Gamma_1 = \pm(\Gamma_0 + \Gamma_2)})$ as shown in the Figs. 5(b)–5(e). They show the critical behavior of curvature function around the multicritical points $MC_{1,2}$, which distinguish between distinct critical phases. The peak of the curvature function tends to diverge as the parameters approach $MC_{1,2}$ from both sides at criticality. Both the criticalities exhibit the universal nature of curvature function around the multicritical points.

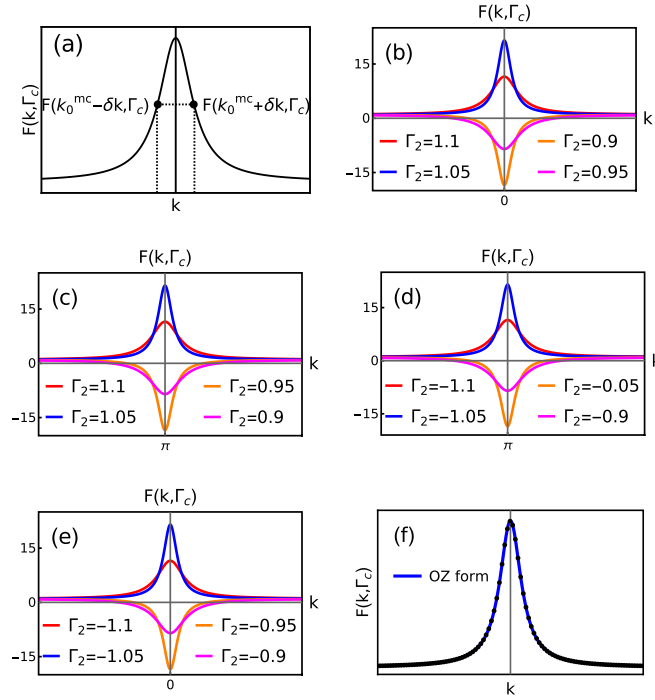

FIG. 5. Curvature function at criticality. (a) Illustration of symmetric nature of curvature function around k_0^{mc}, i.e., $F(k_0^{mc} + \delta k, \mathbf{\Gamma}_c) = F(k_0^{mc} - \delta k, \mathbf{\Gamma}_c)$. (b)–(e) Show the diverging peaks of curvature function as the parameter Γ_2 tend towards the multicritical values $\Gamma_2 = \pm\Gamma_0$ (with $\Gamma_0 = 1$). (b) For MC_1 at $\Gamma_1 = -(\Gamma_0 + \Gamma_2)$. (c) For MC_1 at $\Gamma_1 = (\Gamma_0 + \Gamma_2)$. (d) For MC_2 at $\Gamma_1 = -(\Gamma_0 + \Gamma_2)$. (e) For MC_2 at $\Gamma_1 = (\Gamma_0 + \Gamma_2)$. Flip in the sign of diverging peak is clearly observed as Γ_2 tuned across the multicritical points. The swapping of k_0^{mc} for MC_2 is also evident from (d) and (e). (f) Shows the fitting of Ornstein-Zernike form in Eq. (18) with the data points of curvature function at criticality.

The scenario around MC_1 on the critical line $\Gamma_1 = -(\Gamma_0 + \Gamma_2)$ shows the divergence in curvature function at the $k_0^{mc} = 0$, as shown in Fig. 5(b). As the parameter Γ_2 is tuned towards its multicritical value (i.e., MC_1) on both sides, the diverging peak of curvature function increases leading to a complete divergence at MC_1 and flips sign as the critical value is crossed. This signals the topological transition across MC_1 at criticality. Similar behavior of curvature function can be observed around MC_1 on the critical line $\Gamma_1 = (\Gamma_0 + \Gamma_2)$, for which the divergence occurs at $k_0^{mc} = \pi$, as shown in Fig. 5(c).

The nature of curvature function around MC_2 at both the criticalities share the same property of divergence and flipping of sign as shown in Figs. 5(d) and 5(e). Note that the k_0^{mc} at which the diverging peak increases on approaching the multicritical value is $k_0^{mc} = \pi$ instead of $k_0^{mc} = 0$ for $\Gamma_1 = -(\Gamma_0 + \Gamma_2)$ (and $k_0^{mc} = 0$ instead of $k_0^{mc} = \pi$ for $\Gamma_1 = (\Gamma_0 + \Gamma_2)$). This swapping of k_0^{mc} occurs as a consequence of the intersection of critical lines. Typically the multicritical point MC_2 is the same point for both the critical lines $\Gamma_1 = \pm(\Gamma_0 + \Gamma_2)$ in parameter space. These critical lines intersect each other at MC_2, which results in the swapping of respective k_0^{mc} values.

A. Critical exponents

The condition in Eq. (13) for curvature function allows one to choose the proper gauge for which $F(k, \mathbf{\Gamma})$ can be written in Ornstein-Zernike form around the k_0 [30],

$$F(k_0 + \delta k, \mathbf{\Gamma}) = \frac{F(k_0, \mathbf{\Gamma})}{1 + \xi^2 \delta k^2}, \tag{16}$$

where δk is small deviation from k_0, $F(k_0, \mathbf{\Gamma})$ is the height of the peak and ξ is characteristic length scale or the width of the peak. As we approach critical point, one can also find the divergence in the characteristic length ξ along with the curvature function. The divergences in both $F(k_0, \mathbf{\Gamma})$ and ξ give rise to the critical exponents

$$F(k_0, \mathbf{\Gamma}) \propto |\mathbf{\Gamma} - \mathbf{\Gamma}_c|^{-\gamma}, \quad \xi \propto |\mathbf{\Gamma} - \mathbf{\Gamma}_c|^{-\nu}, \tag{17}$$

where γ and ν are the critical exponents, which define the universality class of the undergoing topological phase transition. These exponents obeys a scaling law, imposed by the conservation of topological invariant, which reads $\gamma = \nu$ for 1D systems [41].

Surprisingly, these scaling behaviors of curvature function also appear at multicriticality by approaching it along the critical lines. Approaching multicritical points $MC_{1,2}$, curvature function acquires Ornstein-Zernike form around k_0^{mc}.

$$F\left(k_0^{mc} + \delta k, \mathbf{\Gamma}_c\right) = \frac{F\left(k_0^{mc}, \mathbf{\Gamma}_c\right)}{1 + \xi_c^2 \delta k^2}, \tag{18}$$

where $\delta k = |k - k_0^{mc}|$, ξ_c is the characteristic length scale at criticality and it represents the width of the curvature function that develops around k_0^{mc} as the parameters $\mathbf{\Gamma}_c \to \mathbf{\Gamma}_{mc}$. The critical behavior of curvature function around the multicritical points $MC_{1,2}$ can be captured by the same exponents γ and ν defined by

$$F\left(k_0^{mc}, \mathbf{\Gamma}_c\right) \propto |\mathbf{\Gamma}_c - \mathbf{\Gamma}_{mc}|^{-\gamma}, \quad \xi_c \propto |\mathbf{\Gamma}_c - \mathbf{\Gamma}_{mc}|^{-\nu}. \tag{19}$$

One can calculate these critical exponents and quantify the scaling properties, numerically, through fitting the diverging peak of curvature function with the Ornstein-Zernike form in Eq. (18), as shown in Fig. 5(f). The data points collected for $F(k_0^{mc}, \mathbf{\Gamma}_c)$ and ξ_c can then be fitted again with the equation of the form in Eq. (19), to extract the exponents γ and ν at the multicritical points. Figures 6(a) and 6(b) show the acquired values of exponents for MC_1 and MC_2, respectively, on approaching from either side. The critical exponents are found to be, $\gamma_{+/-} = \gamma \approx 1$ and $\nu_{+/-} = \nu \approx 1$ for both multicritical points $MC_{1,2}$, where $\gamma_{+(-)}$ and $\nu_{+(-)}$ represents the scaling behavior of curvature function with positive (negative) peaks around the multicritical points on both the criticalities.

The exponents can also be estimated analytically by writing the curvature function in Ornstein-Zernike form (see Appendix D for details). It yields the same values of critical exponents for both $MC_{1,2}$. The exponents calculated obey certain scaling laws and define universality class of the multicriticalities. For topological transition occurring through both the multicritical point $MC_{1,2}$ the exponents are found to have $\gamma = \nu = 1$ both numerically and analytically. The scaling law $\gamma = \nu$ for 1D systems [41] is thus true for the critical behavior of the multicritical points governing the topological transition at criticality.

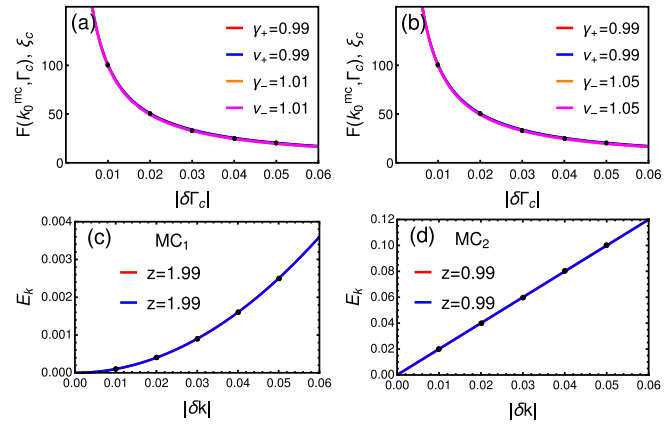

FIG. 6. Critical exponents. (a) and (b) represent exponents of curvature function (γ and ν) for MC_1 and MC_2, respectively. The notation $\gamma_{+/-}$ and $\nu_{+/-}$ represent the exponents on approaching the multicritical points from either sides. Dynamical exponent for (c) MC_1: represents quadratic dispersion and (d) MC_2: represents linear dispersion. Red and blue in (c), (d) correspond to the criticalities $\Gamma_1 = \mp(\Gamma_0 + \Gamma_2)$, respectively.

In addition, the dynamical exponent z dictates the nature of the spectra near the gap closing momenta k_0^{mc}, i.e., $E_k \propto k^z$ [8]. It can be calculated numerically as shown in Figs. 6(c) and 6(d), where the data points around gap closing momenta k_0^{mc} at the multicritical points $MC_{1,2}$ are shown. The spectra is quadratic at MC_1 and linear at MC_2. The quadratic spectra results in the dynamical critical exponent $z \approx 2$, while for linear spectra $z \approx 1$. This behavior is true for both the criticalities. Therefore, the multicriticalities with both $z = 1$ and $z = 2$ favor the topological transition at criticality.

The universality class for the topological transition at criticality through both $MC_{1,2}$ can now be obtained using the set of three critical exponents (γ, ν, z), which captures the scaling behavior around the multicritical points with distinct nature. The universality class of the multicriticality at MC_1 is (1,1,2) and for MC_2 it reads (1,1,1). Therefore, it is clear that the topological transition at quantum criticality occurs through two distinct multicriticalitie,s which belong to different universality classes.

B. Scaling theory

Based on the divergence of the curvature function, a scaling theory has been developed [20,30,30–38]. This is achieved by the deviation reduction mechanism where the deviation of the curvature function from its fixed point configuration can be reduced gradually. In the curvature function $F(k, \mathbf{\Gamma})$, for a given $\mathbf{\Gamma}$ in the parameter space, one can find a new $\mathbf{\Gamma}'$, which satisfies

$$F(k_0, \mathbf{\Gamma}') = F(k_0 + \delta k, \mathbf{\Gamma}), \tag{20}$$

where δk is small deviation away from the k_0, satisfying $F(k_0 + \delta k, \mathbf{\Gamma}) = F(k_0 - \delta k, \mathbf{\Gamma})$. As a consequence of the same topology of the system at $\mathbf{\Gamma}$ and at fixed point $\mathbf{\Gamma}_f$, the curvature function can be written as $F(k, \mathbf{\Gamma}) = F_f(k, \mathbf{\Gamma}_f) + F_d(k, \mathbf{\Gamma}_d)$, where $F_f(k, \mathbf{\Gamma}_f)$ is curvature function at fixed point and $F_d(k, \mathbf{\Gamma}_d)$ is deviation from the fixed point. The

scaling procedure drives the deviation part of curvature function $|F_d(k_0, \mathbf{\Gamma}_d)| \to 0$. The fixed point configuration is invariant under the scaling operation, i.e., $F_f(k_0, \mathbf{\Gamma}_f) = F_f(k_0 + \delta k, \mathbf{\Gamma}_f)$.

Performing the scaling procedure in Eq. (20) iteratively and solving $\mathbf{\Gamma}$ for every deviation δk, one can obtain a renormalization group (RG) equation for the coupling parameters. Expanding Eq. (20) in leading order and writing $\mathbf{\Gamma}' - \mathbf{\Gamma} = d\mathbf{\Gamma}$ and $(\delta k)^2 = dl$, one can obtain a generic RG equation

$$\frac{d\mathbf{\Gamma}}{dl} = \frac{1}{2}\frac{\partial_k^2 F(k, \mathbf{\Gamma})|_{k=k_0}}{\partial_{\mathbf{\Gamma}} F(k_0, \mathbf{\Gamma})}. \tag{21}$$

Since the curvature function diverges at $\mathbf{\Gamma}_c$, the scaling procedure gradually drives the system away from $\mathbf{\Gamma}_c$ towards $\mathbf{\Gamma}_f$ without changing the topological invariant. Thus, eventually, the RG flow distinguishes between distinct gapped phases and correctly captures the topological phase transitions between the gapped phases in the system.

In order to capture the topological transition at criticality one can modify the same scaling scheme to incorporate the multicriticality. This is possible since the qualitative behavior of the curvature function defined at criticality exhibits the same diverging nature near multicritical points with the property $F(k_0^{mc}, \mathbf{\Gamma}'_c) = F(k_0^{mc} + \delta k, \mathbf{\Gamma}_c)$ (here δk is small deviation from k_0^{mc}). As the parameters at criticality $\mathbf{\Gamma}_c \to \mathbf{\Gamma}_{mc}$, the topology of the critical phase changes implying a topological transition at multicritical point.

Based on the divergence of the curvature function at criticality, the scaling theory can be achieved by performing the deviation reduction mechanism at criticality. As a consequence of the same topology of the system at $\mathbf{\Gamma}_c$ and at fixed point $\mathbf{\Gamma}_c^f$, the curvature function can be written as $F(k, \mathbf{\Gamma}_c) = F_f(k, \mathbf{\Gamma}_c^f) + F_d(k, \mathbf{\Gamma}_c^d)$, where $F_f(k, \mathbf{\Gamma}_c^f)$ is the curvature function at fixed point and $F_d(k, \mathbf{\Gamma}_c^d)$ is deviation from the fixed point. For a given $\mathbf{\Gamma}_c$, one can find a new $\mathbf{\Gamma}'_c$, which satisfies $F(k_0^{mc}, \mathbf{\Gamma}'_c) = F(k_0^{mc} + \delta k, \mathbf{\Gamma}_c)$. Iteratively performing this scaling procedure and solving $\mathbf{\Gamma}_c$ for every δk, deviation of curvature function decreases and eventually $F(k, \mathbf{\Gamma}_c) \to F_f(k, \mathbf{\Gamma}_c^f)$.

One can obtain a renormalization group (RG) equation for the coupling parameters using the scaling parameter $\delta k^2 = dl$ and $\mathbf{\Gamma}'_c - \mathbf{\Gamma}_c = d\mathbf{\Gamma}_c$ as

$$\frac{d\mathbf{\Gamma}_c}{dl} = \frac{1}{2}\frac{\partial_k^2 F(k, \mathbf{\Gamma}_c)|_{k=k_0^{mc}}}{\partial_{\mathbf{\Gamma}_c} F\left(k_0^{mc}, \mathbf{\Gamma}_c\right)}. \tag{22}$$

The distinct critical phases with different topological characters can be distinguished from the RG flow of Eq. (22). The multicritical points and fixed points are then easily captured by analyzing the RG flow lines.

$$\begin{aligned}
&\text{Multicritical point:} && \left|\frac{d\mathbf{\Gamma}_c}{dl}\right| \to \infty, && \text{flow directs away.}\\
&\text{Stable fixed point:} && \left|\frac{d\mathbf{\Gamma}_c}{dl}\right| \to 0, && \text{flow directs into.}\\
&\text{Unstable fixed point:} && \left|\frac{d\mathbf{\Gamma}_c}{dl}\right| \to 0, && \text{flow directs away.}
\end{aligned} \tag{23}$$

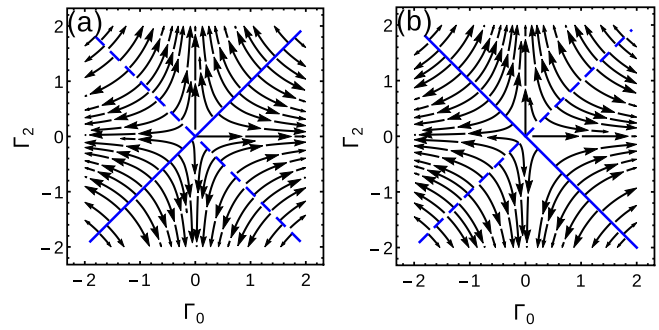

FIG. 7. RG flow diagrams. The multicritical and fixed lines are represented as solid and dashed lines, respectively. (a) For MC_1, where MC_2 appears as unstable fixed line. (b) For MC_2, where MC_1 appears as unstable fixed line. The RG flow lines clearly demonstrates the topological transition at criticality.

Performing the RG scheme to the model at criticality, we obtain the RG equations for MC_1 as

$$\frac{d\Gamma_0}{dl} = \frac{\Gamma_0(\Gamma_0 + \Gamma_2)}{2(\Gamma_0 - \Gamma_2)} \quad \text{and} \quad \frac{d\Gamma_2}{dl} = -\frac{\Gamma_2(\Gamma_0 + \Gamma_2)}{2(\Gamma_0 - \Gamma_2)}. \tag{24}$$

Both the critical lines $\Gamma_1 = \pm(\Gamma_0 + \Gamma_2)$, yield the same RG equations. The multicritical point MC_1 is manifested as a line $\Gamma_0 = \Gamma_2$ with all flow lines flowing away, as shown in Fig. 7(a). The condition in Eq. (23) for multicritical points is satisfied as the flow rate diverges at MC_1, which also indicates that it is the topological phase transition point between critical phases. Surprisingly, $\Gamma_0 = -\Gamma_2$ (MC_2) is obtained as a line of unstable fixed points at which flow rate vanishes with all the flow lines are flowing away.

In order to realize the topological transition at criticality through MC_2 one has to consider the swapping of k_0^{mc}. The RG equation for the critical line $\Gamma_1 = (\Gamma_0 + \Gamma_2)$, has to be derived with $k_0^{mc} = 0$ and vice versa. This procedure yields the RG equations of the form

$$\frac{d\Gamma_0}{dl} = \frac{\Gamma_0(\Gamma_0 - \Gamma_2)}{2(\Gamma_0 + \Gamma_2)} \quad \text{and} \quad \frac{d\Gamma_2}{dl} = -\frac{\Gamma_2(\Gamma_0 - \Gamma_2)}{2(\Gamma_0 + \Gamma_2)}. \tag{25}$$

In this case, $\Gamma_0 = -\Gamma_2$ (MC_2) is obtained to be the topological transition point between critical phases, with the diverging flow rate and flow lines directing away, as shown in Fig. 7(b). The unstable fixed point appear at $\Gamma_0 = \Gamma_2$ (MC_1) with vanishing flow rate and flow lines flowing away.

C. Wannier state correlation function

Along with the RG scheme, a correlation function in terms of Wannier-state representation is proposed to characterize the topological phase transition [41]. This quantity may be measured in higher dimensions [33,42,43]. It is the filled-band contribution to the charge-polarization correlation between Wannier states at different positions, and can be obtained after the Fourier transform of the curvature function. For the two-band model considered here with only the lower band occupied the Wannier state at a distance R,

$$|R\rangle = \int dk e^{ik(\hat{r}-R)}\,|u_k\rangle \tag{26}$$

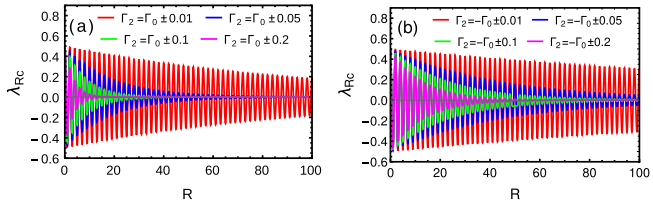

FIG. 8. Wannier-state correlation function at criticality. (a) For MC_1. (b) For MC_2. Approaching the multicritical points $\Gamma_2 = \pm\Gamma_0$ (with $\Gamma_0 = 1$), the decay in the correlation function gets slower on either side of $MC_{1,2}$.

with position operator $\hat{r}$, defines Wannier-state correlation function as the overlap of the states $|0\rangle$ at the origin and at a distance $|R\rangle$, as [41]

$$\lambda_R = \langle R|\hat{r}|0\rangle = \int dk e^{ikR}\langle u_k|i\partial_k|u_k\rangle. \tag{27}$$

Meanwhile, the substitution of the Ornstein-Zernike form of curvature function [Eq. (16)] yields the Wannier-state correlation function λ_R, to be

$$\lambda_R = \int \frac{dk}{2\pi} e^{ikR} F(k, \mathbf{\Gamma}) = e^{ik_0 R}\frac{F(k_0, \mathbf{\Gamma})}{2\xi} e^{-\frac{R}{\xi}}. \tag{28}$$

where ξ can be treated as correlation length of topological phase transition. The correlation function λ_R decays exponentially on either sides of the critical point. The decay gets slower as the parameter is tuned towards criticality.

Surprisingly, this notion of correlation function holds true even at criticality and identify the unique topological phase transition at criticality. The behavior of correlation function evidently show that the topological phase transition occurs at the multicritical points $MC_{1,2}$ at both the criticalities. The Wannier-state correlation function can be calculated at criticality as

$$\lambda_{Rc} = e^{ik_0^{mc} R}\frac{F\left(k_0^{mc}, \mathbf{\Gamma}_c\right)}{2\xi_c} e^{-R/\xi_c}. \tag{29}$$

where $\xi_c = F(k_0^{mc}, \mathbf{\Gamma}_c) = (\Gamma_0 - 3\Gamma_2)/2(\Gamma_2 - \Gamma_0)$ for MC_1. The correlation function decays faster away from the the multicritical point MC_1 and the decay slow down as one approaches MC_1 with the correlation length $\xi_c \to \infty$, as shown in Fig. 8(a). Both the criticalities shows same behavior of correlation function near this multicritical point on both sides indicating that the multicriticality is indeed a topological phase transition point at criticality. Note that the only difference between the criticalities for $k_0 = 0$ and π is the oscillatory behavior of λ_{Rc} originating from the term $e^{ik_0 R}$.

To obtain the critical nature of MC_2 one has to consider the swapping of k_0^{mc} [Eqs. (4) and (5)], which yields $\xi_c = F(k_0^{mc}, \mathbf{\Gamma}_c) = (\Gamma_0 + 3\Gamma_2)/2(\Gamma_0 + \Gamma_2)$. This captures the critical nature of MC_2, where the decay gets slower as one approaches this point from both sides, as shown in Fig. 8(b). Therefore, the behavior of the correlation function evidently shows that the topological phase transition occurs at the multicritical points. For both the criticalities, the correlation length ξ_c coincides with the decay length of the edge modes at criticality studied earlier.

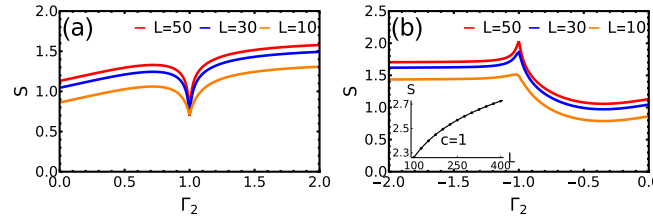

FIG. 9. Entanglement entropy at criticality (with $\Gamma_0 = 1$). Topological transitions are identified with (a) minima at MC_1 ($\Gamma_2 = 1$) and (b) maxima at MC_2 ($\Gamma_2 = -1$). Inset shows scaling of S at MC_2 with central charge $c = 1$.

VI. ENTANGLEMENT ENTROPY

The characteristics of a criticality can be effectively quantified from the entanglement entropy (EE) of the ground state by arbitrarily dividing a system into two subsystems [44–46]. Taking the advantage of Wick's theorem, the eigenvalues of the reduced density matrix can be extracted from the two point correlation matrix, which in the thermodynamic limit can be written as [46]

$$C_{i,j} = \int_{-\pi}^{\pi} \frac{dk}{2\pi} e^{ik(i-j)}\mathcal{G}(k), \quad \text{where} \quad \mathcal{G}(k) = \frac{\boldsymbol{\chi}\cdot\boldsymbol{\sigma}}{E_k}, \tag{30}$$

with $1 \leqslant i, j \leqslant L$ (where L is the subsystem size). The EE (S) can be computed as [46]

$$S = -\frac{1}{2}\sum_{\kappa=\pm,\Lambda_i} \frac{1-\kappa\Lambda_i}{2}\ln\left(\frac{1-\kappa\Lambda_i}{2}\right), \tag{31}$$

where Λ_i are the eigenvalues of correlation matrix. The EE signals the topological transition at the multicritical points, as shown in Fig. 9. The profile of EE shows, maxima at MC_2 [Fig. 9(b)] and surprisingly minima at MC_1 [Fig. 9(a)].

For the generic model in Eq. (1), the MC_1 is the intersection point of fixed and critical lines. Remarkably, at MC_1, we observe that the fixed point characteristic is more dominant, which results in the minima of entanglement entropy, in oppose to the critical point behavior where entanglement is supposed to maximize due to the enhanced correlations (see Appendix E for more details). Besides, at MC_1, the bulk is not a CFT. This can be seen from the multiplicity factor (m), i.e., the degenerate zeros on the unit circle of the complex function associated with the Hamiltonian. The multiplicity at MC_1 is $m = 2$ [see Figs. 4(g)–4(j)]. As shown in Ref. [8], if the complex function has degenerate zeros with multiplicity m, the bulk is not CFT and implies the dynamical exponent $z = m$. This is consistent with z value obtained for MC_1 [see Fig. 6(c)].

At MC_2, the EE is $S = S_0 + (c/3)\log L$ [46] where constant $S_0 = 0.72$ and the central charge $c = 1$ as shown in the inset of Fig. 9(b). The value of c at MC_2 is consistent with Ref. [46], where c was found to be the sum of the central charges of intersecting criticalities. As MC_2 is the intersecting point of the two Ising criticalities ($c = 1/2$), we get $c = 1$.

VII. CONCLUSION

In this work, we reconstruct various tools to characterize the unusual topological phase transitions between distinct crit-

ical phases of an extended model that represents topological insulators and superconductors at criticality. Bound state solutions of the Dirac equation and winding number defined for criticality show that the transitions between the critical phases occur through multicritical points $MC_{1,2}$ of different universality classes as captured through the critical exponents obtained from the divergence of the curvature function. There exists an interesting swapping behavior of the critical momenta k_0^{mc} at MC_2, which manifests in the behavior of curvature function. A scaling theory based on the curvature function unravels that the transitions at $MC_{1,2}$ can be efficiently identified from the RG flow in the parameter space and also shows that, MC_2 manifests as unstable fixed line of RG flow for MC_1 and vice versa. A diverging correlation length obtained from the Wannier-state correlation function, which essentially is the Fourier transform of the curvature function, indicates the occurrences of topological phase transitions at $MC_{1,2}$. Moreover, the unique transitions at $MC_{1,2}$ are characterized with the minima and maxima of entanglement entropy, respectively, revealing an intriguing dominance of the fixed point over the criticality at MC_1.

Our proposed framework, in general, can be applied to the driven systems and higher-dimensional systems. A unique advantage of having topological nontrivial criticalities is that the quantum information remains robust upon tuning the system towards it [9]. By identifying the multicritical points one can choose a proper criticality to tune into and avoid the decoherence due to bulk gap closing and opening. Our topological model at criticality can be simulated with a good control over the tunable parameters in the suitable experimental platforms, which include the superconducting circuit with a single qubit [47,48] and the ultracold atoms mimicking the topological models [49–53], especially the Kitaev model with controlled NN and NNN couplings [51,54,55].

ACKNOWLEDGMENTS

We would like to thank Wei Chen, Griffith M. Rufo, Ruben Verresen, Yuanzhen Chen, Aditi Mitra, Vinod N. Rao, Randeep N. C. for the useful discussions. R.R.K., Y.R.K., and R.S. would like to acknowledge DST (Department of Science and Technology, Government of India, EMR/2017/000898 and CRG/2021/00996) and AMEF (Admar Mutt Education Foundation) for the funding and support. N.R. acknowledges Indian Institute of Science (IISc.), Bangalore for support through the Institution of Eminence (IoE) Post-Doc program. This research was supported in part by the International Centre for Theoretical Sciences (ICTS) during a visit for participating in the program - Novel phases of quantum matter (Code: ICTS/topmatter2019/12).

APPENDIX A: PHYSICAL RELEVANCE OF MODEL HAMILTONIAN

The model considered in Eq. (1) is a generic two-band model for spinless fermions in 1D lattice with nearest-neighbor (NN) and next-nearest-neighbor (NNN) coupling amplitudes of electrons. It maps into extended Su-Schrieffer–Heeger (SSH) [21,23] and Kitaev chains [22,24] in momentum space, which are the simplest 1D models for topological insulators and superconductors, respectively. The tight-binding Hamiltonians can be written as

$$H_{SSH} = \alpha_0 \sum_i c_{i,a}^\dagger c_{i,b} + \alpha_1 \sum_{\langle ij \rangle} (c_{i,a}^\dagger c_{j,b} + \text{H.c.}) + \alpha_2 \sum_{\langle\langle ij \rangle\rangle} (c_{i,a}^\dagger c_{j,b} + \text{H.c.}), \tag{A1}$$

$$H_{\text{Kitaev}} = \beta_0 \sum_i (2c_i^\dagger c_i - 1) - \beta_1 \sum_{\langle ij \rangle} (c_i^\dagger c_j + c_i^\dagger c_j^\dagger + \text{H.c.}) - \beta_2 \sum_{\langle\langle ij \rangle\rangle} (c_i^\dagger c_j + c_i^\dagger c_j^\dagger + \text{H.c.}), \tag{A2}$$

where $c_{i,j}^\dagger$ and $c_{i,j}$ are the fermionic creation and annihilation operators. In H_{SSH}, the subscripts a, b denote the sublattices, with on-site potential α_0 and NN (NNN) hopping amplitude $\alpha_{1(2)}$. In H_{Kitaev}, β_0 is on-site potential and $\beta_{1(2)}$ is NN (NNN) pairing and hopping amplitudes.

The Hamiltonians can be readily diagonalized by Fourier transformation to obtain a generalized Bloch Hamiltonian in the basis of spinor ψ_k

$$H_{SSH} = \sum_k \psi_k^\dagger \mathcal{H}_{SSH} \psi_k \quad \text{with} \quad \psi_k = (c_{a,k} \quad c_{b,k})^T \tag{A3}$$

The Hamiltonian $\mathcal{H}_{SSH}(k) = \chi_x.\sigma_x + \chi_y.\sigma_y$, where $\chi_x = \alpha_0 + \alpha_1 \cos k + \alpha_2 \cos 2k$ and $\chi_y = \alpha_1 \sin k + \alpha_2 \sin 2k$. The excitation spectra can be obtained as $E_k = \pm\sqrt{\chi_x^2 + \chi_y^2}$. The gap closing points (i.e., $E_k = 0$) for a specific k_0 defines critical surfaces or phase boundaries, which separate topologically distinct gapped phases. The gapless edge excitations of these gapped phases are quantified in terms of winding number w, which counts the number of edge modes present in the corresponding gapped phases. There are three critical surfaces for extended SSH model. Two of them are with high-symmetry nature (i.e., $k_0 = -k_0$), $\alpha_1 = -(\alpha_0 + \alpha_2)$ and $\alpha_1 = (\alpha_0 + \alpha_2)$, respectively, for $k_0 = 0$ and π. One with non-high-symmetry nature (i.e., $k_0 \neq -k_0$), $\alpha_0 = \alpha_2$ for $k_0 = \cos^{-1}(-\alpha_1/2\alpha_2)$. Without loss of generality, we assume $\alpha_0 = 1$, hence critical surfaces and multicritical lines will be critical lines and multicritical points, respectively, on the $\alpha_1 - \alpha_2$ plane, as shown in Fig. 10(a). The three critical lines distinguish the gapped phases with invariant number $w = 0, 1, 2$. There are three multicritical points named MC_1 (two of them) and MC_2, with distinct nature, at which the critical lines meet [56].

The edge mode remains localized at the criticalities (critical lines) between the topological nontrivial gapped phases ($w = 1$ and $w = 2$), which give rise to the topological characteristics to the criticality. The same does not occur at the criticality between trivial and nontrivial gapped phases ($w = 0$ and $w = 1$). This results in the criticality to get separated into two distinct critical phases with trivial and nontrivial topological properties. The multicritical points $MC_{1,2}$, with quadratic (i.e., $E_k \propto k^2$) and linear dispersions (i.e., $E_k \propto k$), respectively, facilitates the topological transition at criticality between trivial and nontrivial critical phases.

Similar qualitative behavior can also be observed in the extended Kitaev model due to the striking similarity in the phase diagram with SSH model. For the Kitaev model one

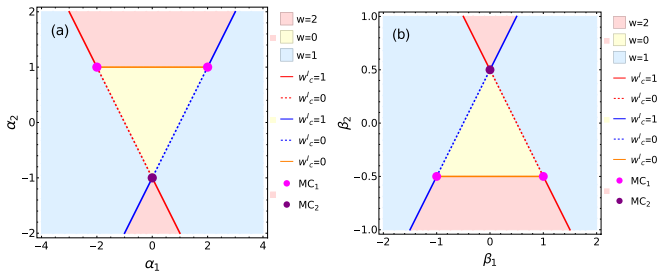

FIG. 10. Topological phase diagrams of (a) extended SSH model (for $\alpha_0 = 1.$) and (b) extended Kitaev model (for $\beta_0 = 0.5$). High symmetry critical lines for $k_0 = 0$ and π are represented in red and blue, respectively, while non-high-symmetry critical lines are in orange. The topological trivial and nontrivial critical phases are represented in dashed and solid lines, respectively. The w_c^I are the winding numbers at criticality [Eq. (10)]. The critical phases are separated by multicritical points MC_1 (magenta dots) and MC_2 (purple dots). Each high symmetry criticality allows topological transition between distinct critical phases through multicritical points.

can obtain

$$H_{\text{Kitaev}} = \sum_k \psi_k^\dagger \mathcal{H}_{Kitaev} \psi_k \quad \text{with} \quad \psi_k = (c_k \quad c_{-k}^\dagger)^T. \tag{A4}$$

The Hamiltonian $\mathcal{H}_{Kitaev}(k) = \chi_x.\sigma_x + \chi_y.\sigma_y$, where $\chi_x = 2\beta_0 - 2\beta_1 \cos k - 2\beta_2 \cos 2k$ and $\chi_y = 2\beta_1 \sin k + 2\beta_2 \sin 2k$, after a rotation along σ_y. The gap closing critical surfaces for this case are $\beta_1 = -(\beta_0 - \beta_2)$, $\beta_1 = (\beta_0 - \beta_2)$ and $\beta_0 = -\beta_2$, respectively, for $k_0 = 0$, $k_0 = \pi$, and $k_0 = \cos^{-1}(-\beta_1/2\beta_2)$. These phase boundaries separate the gapped phases with invariant numbers $w = 0, 1, 2$ as shown in Fig. 10(b) (for $\beta_0 = 0.5$). Localized edge modes living at the criticalities between the nontrivial topological gapped phases can be observed here as well, which define trivial and nontrivial critical phases with distinct topological properties. The multicritical points $MC_{1,2}$ mediate the topological transition at criticality between critical phases with distinct topological nature and share the same properties as in the case of SSH model.

To study the unusual topological transition at criticalities we consider a generic model, which essentially summarize both SSH and Kitaev model, thereby giving one platform to study both topological insulator and superconductor models in one dimension. We define a generalized Bloch Hamiltonian for two-band model by setting $\alpha_0 = 2\beta_0 = \Gamma_0$, $\alpha_1 = -2\beta_1 = \Gamma_1$, and $\alpha_2 = -2\beta_2 = \Gamma_2$. This model captures the physics of both SSH and Kitaev models, especially the phenomenon of multicriticality and the corresponding topological transition.

APPENDIX B: NUMERICAL RESULTS OF EDGE MODES AND TOPOLOGICAL TRANSITION AT CRITICALITY

We begin by discussing the behavior of the pseudo-spin-vectors to identify the trivial and nontrivial criticalities. The characteristic feature of the parameter space curve at criticality is that it passes through the origin while tracing closed curve. Nontrivial critical phases can be identified with the emergence of secondary loops, which encircle the origin indicating a finite winding number or edge modes at criticality,

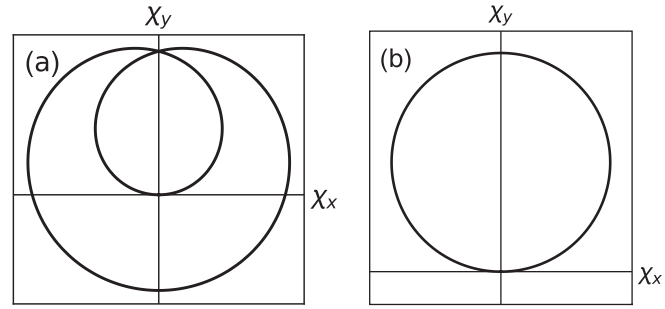

FIG. 11. Pseudo-spin-vector at criticality. (a) Nontrivial critical phase. (b) Trivial critical phase.

as shown in Fig. 11(a). In trivial critical phase parameter space curves always passes through the origin without encircling loops, thus there is no edge modes at criticality, as shown in Fig. 11(b).

Numerical diagonalization of the Hamiltonians in Eq. (A1) and Eq. (A2) (the results shown in this section summarizes both SSH and Kitaev model in open boundary condition) reveals that for the nontrivial critical phases the probability of wave function significantly distributes at the edge of the finite open chain representing the stable localized edge modes, as shown in Fig. 12(a). The corresponding eigenvalue distribution shows two of the eigenvalues trapped at zero

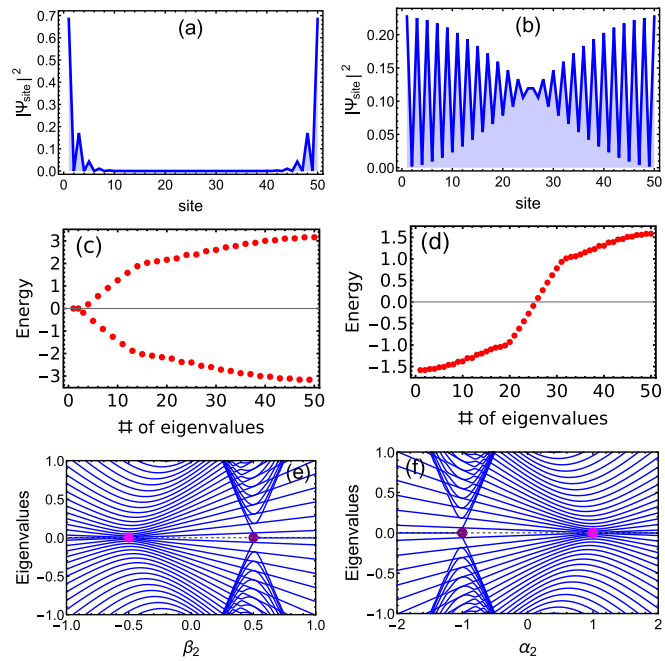

FIG. 12. Numerical results for edge mode and topological phase transition at criticality. Probability distribution at (a) nontrivial critical phase and (b) trivial critical phase. Eigenvalue distribution at (c) nontrivial critical phase and (d) trivial critical phase. Energy spectra at criticalities with respect to the parameters: (e) β_2 (for critical Kitaev model) and (f) α_2 (for critical SSH model). The multicritical points are represented as magenta and purple dots. Zero-energy states are present at nontrivial critical phases and absent at trivial critical phase. The multicritical points differentiate the trivial and nontrivial phases.

energy even if there is no bulk gap, as shown in Fig. 12(c). In case of the trivial critical phase, probability distribution can be found delocalized over the entire system, as shown in Fig. 12(b). Correspondingly, there are no eigenvalues living at zero energy, as shown in Fig. 12(d). The localization and delocalization of the edge modes change across the multicritical points $MC_{1,2}$, which thus differentiate between trivial and nontrivial critical phases.

The topological transition among the nontrivial and trivial critical phases can be identified in the energy spectrum with the system parameter. The presence (absence) of zero-energy states dictates the nontriviality (triviality) with respect to the system parameter, as shown in Figs. 12(e) and 12(f). Note that there is no bulk gap in the spectrum since the system is at criticality. The zero-energy states represent localized stable edge modes living at the critical phases. The transition among the trivial and nontrivial phases can be seen at the multicritical points.

APPENDIX C: BOUND STATE SOLUTION OF DIRAC EQUATION FOR GAPPED PHASES

The model Hamiltonian in Eq. (1) can be recast in the form of Dirac Hamiltonian in one dimension, which represents the topological insulator and superconductor models. The Dirac Hamiltonian of the model can be obtained by the second-order expansion of $\boldsymbol{\chi}$ around the gap closing momenta k_0

$$\mathcal{H}(k) \approx (m - \epsilon_1 k^2)\sigma_x + \epsilon_2 k \sigma_y. \tag{C1}$$

For $k_0 = 0$ we have $m = (\Gamma_0 + \Gamma_1 + \Gamma_2)$, $\epsilon_1 = (\Gamma_1 + 4\Gamma_2)/2$, and $\epsilon_2 = (\Gamma_1 + 2\Gamma_2)$. For $k_0 = \pi$, $m = (\Gamma_0 - \Gamma_1 + \Gamma_2)$, $\epsilon_1 = (4\Gamma_2 - \Gamma_1)/2$, and $\epsilon_2 = (2\Gamma_2 - \Gamma_1)$. The continuum version of the model reads (with $\hbar = 1$)

$$\mathcal{H}(-i\partial_x) \approx \left(m + \epsilon_1 \partial_x^2\right)\sigma_x + (-i\epsilon_2 \partial_x)\sigma_y. \tag{C2}$$

To obtain zero-energy solution $\mathcal{H}\psi(x) = 0$, we multiply σ_y from right-hand side. This implies the wave function $\psi(x) = \rho_\eta \phi(x)$, is an eigenstate of $\sigma_z \rho_\eta = \eta \rho_\eta$. The resulting second-order differential equation can be written as

$$\partial_x^2 \phi(x) = \frac{-(\epsilon_2 \partial_x + \eta m)\phi(x)}{\eta \epsilon_1}. \tag{C3}$$

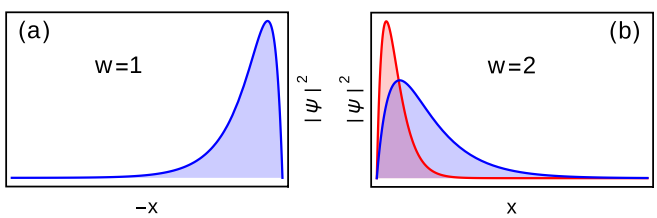

FIG. 13. Bound state solution of Dirac equation for gapped phases. (a) Represents the gapped phase with one edge mode $w = 1$. (b) Represents the gapped phase with two edge modes $w = 2$. Edge modes solutions are localized at the boundary with the localization length $\xi_\pm$.

We set the trial wave function $\phi(x) \propto e^{x/\xi}$ to obtain the secular equation, which yields the inverse of the decay length

$$\xi_+^{-1} \approx -\frac{m}{|\epsilon_2|}. \tag{C4}$$

The decay length is positive if $m < 0$, which identifies the gapped topological nontrivial phase with $w = 1$. Similarly, topological phase with $w = 2$ can also be identified by using the ansatz $\phi(x) \propto e^{-x/\xi}$, which under the condition $m\epsilon_1 > 0$ yields the decay length $\xi_- \approx |\epsilon_2|/m$. The decay length is positive if $m > 0$. Even though, the topological trivial phase with $w = 0$ is also identified with $m > 0$, it does not host any zero-energy solution since the region $m > 0$ for trivial phase satisfies the relation $m\epsilon_1 < 0$. If the parameter $m\epsilon_1 < 0$, spin distribution of the ground state does not show antiparallel spin orientation in momentum space [27]. If $m\epsilon_1 > 0$ is satisfied, spin orientation aligns in the opposite directions with the increasing momentum. Thus the gapped phases $w = 2$ and $w = 0$ are identified with the condition $m\epsilon_1 \lessgtr 0$, respectively. The wave function for zero-energy solution can be derived to be

$$\psi(x) \propto \psi(0)(e^{\pm x/\xi_+} - e^{\pm x/\xi_-}), \tag{C5}$$

up to normalization constant. The solution is exponentially localized near the boundary, as shown in Fig. 13.

APPENDIX D: ANALYTICAL EVALUATION OF CRITICAL EXPONENTS

The critical exponents in Sec. V A can also be estimated analytically by writing the curvature function [Eq. (15)] in Ornstein-Zernike form. It can be achieved by expanding the pseudo-spin-vector $\boldsymbol{\chi}(k)$ around k_0^{mc} up to third order.

$$\boldsymbol{\chi}(k)|_{k=k_0^{mc}} \approx \boldsymbol{\chi}\left(k_0^{mc}\right) + \partial_k \boldsymbol{\chi}\left(k_0^{mc}\right)\delta k + \frac{\partial_k^2 \boldsymbol{\chi}\left(k_0^{mc}\right)}{2}\delta k^2. + \frac{\partial_k^3 \boldsymbol{\chi}\left(k_0^{mc}\right)}{6}\delta k^3, \tag{D1}$$

Expansion of the individual components of the vectors $\chi_x(k)|_{k=k_0^{mc}} = \Gamma_0(1 \pm \cos k) + \Gamma_2(\cos 2k \pm \cos k)$ and $\chi_y(k)|_{k=k_0^{mc}} = \Gamma_2(\sin 2k \pm \sin k) \pm \Gamma_0 \sin k$ for both the criticalities of the model yields

$$\text{For } MC_1: \quad \chi_x(k)|_{k=k_0^{mc}} \approx \frac{(\Gamma_0 - 3\Gamma_2)}{2}\delta k^2. \tag{D2}$$

$$\chi_y(k)|_{k=k_0^{mc}} \approx (\Gamma_2 - \Gamma_0)\delta k + \frac{\Gamma_0 - 7\Gamma_2}{6}\delta k^3. \tag{D3}$$

$$\text{For } MC_2: \quad \chi_x(k)|_{k=k_0^{mc}} \approx (\Gamma_0 + 3\Gamma_2)\delta k. \tag{D4}$$

$$\chi_y(k)|_{k=k_0^{mc}} \approx 2(\Gamma_2 + \Gamma_0) + \frac{\Gamma_0 + 5\Gamma_2}{2}\delta k^2. \tag{D5}$$

The expression for MC_2 is obtained after considering the swapping of k_0^{mc}. The Ornstein-Zernike form of the curvature

function for MC_1 can be obtained as

$$F(k,\delta\mathbf{\Gamma}_c) = \frac{\chi_y\partial_k\chi_x - \chi_x\partial_k\chi_y}{\chi_x^2+\chi_y^2} = \frac{\left(\frac{A\delta\mathbf{\Gamma}_c\delta k^2 - AB\delta k^4}{\delta\mathbf{\Gamma}_c^2\delta k^2}\right)}{1+\left(\frac{A^2+2\delta\mathbf{\Gamma}_cB}{\delta\mathbf{\Gamma}_c^2}\right)\delta k^2+\left(\frac{B^2}{\delta\mathbf{\Gamma}_c^2}\right)\delta k^4} = \frac{F\left(k_0^{mc},\delta\mathbf{\Gamma}_c\right)}{1+\xi_c^2\delta k^2+\xi_c^4\delta k^4}, \tag{D6}$$

where $\delta\mathbf{\Gamma}_c = |\mathbf{\Gamma}_c - \mathbf{\Gamma}_{mc}| = (\Gamma_2 - \Gamma_0)$, $A = (\Gamma_0 - 3\Gamma_2)/2$, and $B = (\Gamma_0 - 7\Gamma_2)/6$. Similarly, for MC_2 it reads

$$F(k,\delta\mathbf{\Gamma}_c) = \frac{\chi_y\partial_k\chi_x - \chi_x\partial_k\chi_y}{\chi_x^2+\chi_y^2} = \frac{\left(\frac{A\delta\mathbf{\Gamma}_c - AB\delta k^2}{\delta\mathbf{\Gamma}_c^2}\right)}{1+\left(\frac{A^2+2\delta\mathbf{\Gamma}_cB}{\delta\mathbf{\Gamma}_c^2}\right)\delta k^2+\left(\frac{B^2}{\delta\mathbf{\Gamma}_c^2}\right)\delta k^4} = \frac{F\left(k_0^{mc},\delta\mathbf{\Gamma}_c\right)}{1+\xi_c^2\delta k^2+\xi_c^4\delta k^4}, \tag{D7}$$

where $\delta\mathbf{\Gamma}_c = 2(\Gamma_2+\Gamma_0)$, $A = (\Gamma_0+3\Gamma_2)$, and $B = (\Gamma_0 + 5\Gamma_2)/2$. Now the critical exponents can be obtained using Eq. (19). The exponent γ is given by

$$F\left(k_0^{mc},\delta\mathbf{\Gamma}_c\right) = A\delta\mathbf{\Gamma}_c^{-1} \Rightarrow \gamma = 1. \tag{D8}$$

Exponent ν can be obtained by identifying the dominant term among the coefficients of δk^2 and δk^4. It can be easily seen that approaching multicritical points $MC_{1,2}$ on both the criticalities yields $A > \sqrt{2B}, \sqrt{B}$. This implies

$$\xi_c = A\delta\mathbf{\Gamma}_c^{-1} \Rightarrow \nu = 1. \tag{D9}$$

Thus both the numerical and analytical methods yield the same values of critical exponents for topological transition through multicritical points at criticality.

APPENDIX E: ENTANGLEMENT ENTROPY AT CRITICAL AND FIXED POINTS

In order to understand the behavior of EE at the multicritical point MC_1, at first, we show MC_1 is the intersection point of fixed and critical lines in the parameter space. The fixed lines can be obtained by performing the curvature function renormalization group method [30], to capture the topological transition between gapped phases of the generic model in Eq. (1), in $\Gamma_1-\Gamma_2$ plane with $\Gamma_0 = 1$. There are two high-symmetry critical lines $\Gamma_2 = (-\Gamma_0 \mp \Gamma_1)$ for $k_0 = 0, \pi$, respectively. The CRG equations can be obtained as

$$\frac{d\Gamma_1}{dl} = -\frac{\Gamma_1(\Gamma_2\mp\Gamma_1)+\Gamma_0(\Gamma_1\pm 8\Gamma_2)}{\Gamma_0\pm\Gamma_1+\Gamma_2}, \tag{E1}$$

$$\frac{d\Gamma_2}{dl} = \mp\frac{(\Gamma_0-\Gamma_2)[\Gamma_1(\Gamma_2\mp\Gamma_1)+\Gamma_0(\Gamma_1\pm 8\Gamma_2)]}{(2\Gamma_0\pm\Gamma_1)(\Gamma_0\pm\Gamma_1+\Gamma_2)}, \tag{E2}$$

where the upper and lower signs are for $k_0 = 0, \pi$, respectively. The critical and fixed lines can be obtained from the CRG equations using the conditions $|d\mathbf{\Gamma}/dl| \to \infty$ and $|d\mathbf{\Gamma}/dl| \to 0$, respectively [32], and are depicted in Fig. 14(a). From the CRG equations for $k_0 = 0$, the fixed line can be obatined as $\Gamma_2 = (\Gamma_1^2 - \Gamma_0\Gamma_1)/(8\Gamma_0+\Gamma_1)$ (purple line), which intersects the critical line $\Gamma_2 = -(\Gamma_0+\Gamma_1)$ (red line) at the multicritical point $(\Gamma_1,\Gamma_2) = (-2,1)$. Similarly, from the CRG equations for $k_0 = \pi$, the fixed line $\Gamma_2 = (\Gamma_1^2+\Gamma_0\Gamma_1)/(8\Gamma_0-\Gamma_1)$ (green line) is obtained and it intersects the critical line $\Gamma_2 = (-\Gamma_0+\Gamma_1)$ (blue line) at the multicritical point $(\Gamma_1,\Gamma_2) = (2,1)$. Both the multicritical points $(\Gamma_1,\Gamma_2) = (\pm 2,1)$ are of type MC_1 as explained in Fig. 10. Therefore, it is clear that the MC_1 is the intersection point of fixed and critical lines.

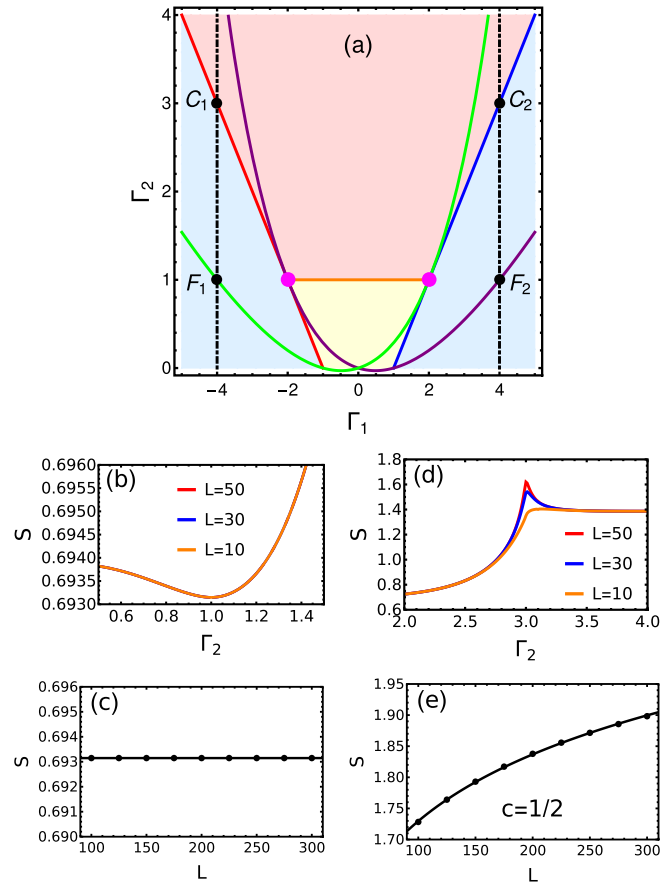

FIG. 14. EE at critical and fixed points. (a) Phase diagram of the model in Eq. (1) [same as in Fig. 10(a)]. It is plotted in $\Gamma_1-\Gamma_2$ plane with $\Gamma_0 = 1$. The critical lines are represented as blue, red, and orange lines. The multicritical points MC_1 are the magenta dots at $(\Gamma_1,\Gamma_2) = (\pm 2, 1)$. These points are the intersection points of the fixed lines (represented in green and purple) and high-symmetry critical lines (red and blue lines). To see the EE profile at fixed and critical points, we choose two paths at $\Gamma_1 = \pm 4$ (black dashed lines). The points C_1, C_2 and F_1, F_2 are the critical and fixed points, respectively, along the two paths. The behavior of critical (fixed) points C_1 (F_1) and C_2 (F_2) are identical, therefore only the plots for C_1 and F_1 are shown. (b) Variation EE with parameter in the vicinity of F_1 ($\Gamma_1 = -4, \Gamma_2 = 1$) for different subsystem sizes. (c) Scaling of EE at the fixed point F_1 the subsystem size L. (d) EE in the vicinity of the point C_1 i.e. ($\Gamma_1 = -4, \Gamma_2 = 3$). (e) Scaling of EE at the critical point C_1. The EE increases with the subsystem size as $S = S_0 + (c/3)\log(L)$ where the constant $S_0 = 1.01$ and central charge $c = 1/2$ representing Ising criticalities.

The EE shows minima at a fixed point in contrast to a critical point (where the EE is maximum), as shown in Figs. 14(b)–14(e). We choose two vertical paths in the parameter space at $\Gamma_1 = \pm 4$, as shown in Fig. 14(a). The paths intersect the critical points at C_1, C_2 (i.e., at $\Gamma_2 = 3$) and fixed points at F_1, F_2 (i.e., at $\Gamma_2 = 1$). The EE shows minima as a consequence of minimal correlations at the fixed points, as shown in Fig. 14(b) and subsytem-size independence at the fixed points, Fig. 14(c). Similarly, the maximum correlations yield the maxima at the critical points, as shown in Fig. 14(d). Moreover, at the critical points the EE is $S = S_0 + (c/3)\log L$ where 'c' is the central charge of the CFT and S_0 is a constant. Figure 14(e) shows the scaling of EE at C_1 and C_2 with $c = 1/2$, representing Ising criticality [9]. In contrast, the fixed points F_1 and F_2 are in the gapped phase and the EE remains constant with subsystem size L representing the area law, as shown in Fig. 14(c). This demonstrates the distinction between fixed and critical points in terms of EE and its scaling.

[1] F. D. M. Haldane, Phys. Rev. Lett. **61**, 2015 (1988).
[2] C. L. Kane and E. J. Mele, Phys. Rev. Lett. **95**, 226801 (2005).
[3] P. Narang, C. A. C. Garcia, and C. Felser, Nature Mater. **20**, 293 (2021).
[4] J. Wang and S.-C. Zhang, Nature Mater. **16**, 1062 (2017).
[5] D. J. Thouless, M. Kohmoto, M. P. Nightingale, and M. den Nijs, Phys. Rev. Lett. **49**, 405 (1982).
[6] M. Z. Hasan and C. L. Kane, Rev. Mod. Phys. **82**, 3045 (2010).
[7] M. A. Continentino, S. Rufo, and G. M. Rufo, Finite size effects in topological quantum phase transitions, *Strongly Coupled Field Theories for Condensed Matter and Quantum Information Theory*, Springer Proceedings in Physics 239 (Springer, Berlin, 2020).
[8] R. Verresen, N. G. Jones, and F. Pollmann, Phys. Rev. Lett. **120**, 057001 (2018).
[9] R. Verresen, R. Thorngren, N. G. Jones, and F. Pollmann, Phys. Rev. X **11**, 041059 (2021).
[10] N. G. Jones and R. Verresen, J. Stat. Phys. **175**, 1164 (2019).
[11] R. Verresen, arXiv:2003.05453 v1 [cond-mat.str-el].
[12] S. Rahul, R. R. Kumar, Y. R. Kartik, and S. Sarkar, J. Phys. Soc. Jpn. **90**, 094706 (2021).
[13] S. Niu, Y. Wang, and X.-J. Liu, arXiv:2106.13400 v2 [cond-mat.str-el].
[14] R. Thorngren, A. Vishwanath, and R. Verresen, Phys. Rev. B **104**, 075132 (2021).
[15] O. Balabanov, D. Erkensten, and H. Johannesson, Phys. Rev. Res. **3**, 043048 (2021).
[16] J. Fraxanet, D. González-Cuadra, T. Pfau, M. Lewenstein, T. Langen, and L. Barbiero, Phys. Rev. Lett. **128**, 043402 (2022).
[17] A. Keselman and E. Berg, Phys. Rev. B **91**, 235309 (2015).
[18] T. Scaffidi, D. E. Parker, and R. Vasseur, Phys. Rev. X **7**, 041048 (2017).
[19] C. M. Duque, H.-Y. Hu, Y.-Z. You, V. Khemani, R. Verresen, and R. Vasseur, Phys. Rev. B **103**, L100207 (2021).
[20] R. R. Kumar, Y. R. Kartik, S. Rahul, and S. Sarkar, Sci. Rep. **11**, 1 (2021).
[21] W. P. Su and J. R. Schrieffer, and A. J. Heeger, Phys. Rev. Lett. **42**, 1698 (1979).
[22] A Y. Kitaev, Phys. Usp. **44**, 131 (2001).
[23] H.-C. Hsu and T.-W. Chen, Phys. Rev. B **102**, 205425 (2020).
[24] Y. Niu, S. B. Chung, C.-H. Hsu, I. Mandal, S. Raghu, and S. Chakravarty, Phys. Rev. B **85**, 035110 (2012).
[25] R. Jackiw and C. Rebbi, Phys. Rev. D **13**, 3398 (1976).
[26] J. Lu, W.-Y. Shan, H.-Z. Lu, and S.-Q. Shen, New J. Phys. **13**, 103016 (2011).
[27] S.-Q. Shen, *Topological Insulators: Dirac Equation in Condensed Matter* (Springer, Berlin, 2018).
[28] G. Zhang and Z. Song, Phys. Rev. Lett. **115**, 177204 (2015).
[29] R. R. Kumar, Y. R. Kartik, and S. Sarkar, arXiv:2211.03320 [cond-mat.str-el].
[30] W. Chen, J. Phys.: Condens. Matter **28**, 055601 (2016).
[31] W. Chen, M. Sigrist, and A. P. Schnyder, J. Phys.: Condens. Matter **28**, 365501 (2016).
[32] W. Chen, Phys. Rev. B **97**, 115130 (2018).
[33] W. Chen and A. P. Schnyder, New J. Phys. **21**, 073003 (2019).
[34] P. Molignini, W. Chen, and R. Chitra, Phys. Rev. B **98**, 125129 (2018).
[35] P. Molignini, W. Chen, and R. Chitra, Phys. Rev. B **101**, 165106 (2020).
[36] F. Abdulla, P. Mohan, and S. Rao, Phys. Rev. B **102**, 235129 (2020).
[37] M. Malard, H. Johannesson, and W. Chen, Phys. Rev. B **102**, 205420 (2020).
[38] P. Molignini, R. Chitra, and W. Chen, Europhys. Lett. **128**, 36001 (2020).
[39] S. Rufo, N. Lopes, M. A. Continentino, and M. A. R. Griffith, Phys. Rev. B **100**, 195432 (2019).
[40] Y. R. Kartik, R. R. Kumar, S. Rahul, N. Roy, and S. Sarkar, Phys. Rev. B **104**, 075113 (2021).
[41] W. Chen, M. Legner, A. Rüegg, and M. Sigrist, Phys. Rev. B **95**, 075116 (2017).
[42] D. A. Abanin, T. Kitagawa, I. Bloch, and E. Demler, Phys. Rev. Lett. **110**, 165304 (2013).
[43] L. Duca, T. Li, M. Reitter, I. Bloch, and M. Schleier-Smith, and U. Schneider, Science **347**, 288 (2015).
[44] G. Vidal, J. I. Latorre, and E. Rico, and A. Kitaev, Phys. Rev. Lett. **90**, 227902 (2003).
[45] F. Pollmann, S. Mukerjee, A. Turner, and J. E. Moore, Phys. Rev. Lett. **102**, 255701 (2009).
[46] D. Yates, Y. Lemonik, and A. Mitra, Phys. Rev. Lett. **121**, 076802 (2018).
[47] Z. Tao, T. Yan, W. Liu, J. Niu, Y. Zhou, L. Zhang, H. Jia, W. Chen, S. Liu, Y. Chen, and D. Yu, Phys. Rev. B **101**, 035109 (2020).
[48] J. Niu, T. Yan, Y. Zhou, Z. Tao, X. Li, W. Liu, L. Zhang, H. Jia, S. Liu, Z. Yan *et al.*, Sci. Bull. **66**, 1168 (2021).
[49] N. Goldman, J. C. Budich, and P. Zoller, Nature Phys. **12**, 639 (2016).
[50] E. J. Meier, F. A. An, and B. Gadway, Nature Commun. **7**, 13986 (2016).

[51] F. A. An, E. J. Meier, and B. Gadway, Phys. Rev. X **8**, 031045 (2018).

[52] D. Xie, W. Gou, T. Xiao, B. Gadway, and B. Yan, npj Quantum Inf. **5**, 55 (2019).

[53] E. J. Meier, F. A. An, A. Dauphin, M. Maffei, P. Massignan, T. L. Hughes, and B. Gadway, Science **362**, 929 (2018).

[54] L. Jiang, T. Kitagawa, J. Alicea, A. Akhmerov, D. Pekker, G. Refael, J. I. Cirac, E. Demler, M. D. Lukin, and P. Zoller, Phys. Rev. Lett. **106**, 220402 (2011).

[55] C. V. Kraus, S. Diehl, P. Zoller, and M. A. Baranov, New J. Phys. **14**, 113036 (2012).

[56] M. Malard, D. Brandao, P. E. de Brito, and H. Johannesson, Phys. Rev. Res. **2**, 033246 (2020).